Microgel-based etalon membranes
Characterization and properties

Kontaxi, G.; Wensink, G.; Sberna, P. M.; Rücker, M.; Garbin, V.; Serpe, M. J.; Bazyar, H.

DOI
10.1063/5.0227483

Publication date
2024

Document Version
Final published version

Published in
APL Materials

Citation (APA)
Kontaxi, G., Wensink, G., Sberna, P. M., Rücker, M., Garbin, V., Serpe, M. J., & Bazyar, H. (2024). Microgel-based etalon membranes: Characterization and properties. *APL Materials*, *12*(9), Article 091113. https://doi.org/10.1063/5.0227483

APL Materials

RESEARCH ARTICLE | SEPTEMBER 13 2024

Microgel-based etalon membranes: Characterization and properties

G. Kontaxi ; G. Wensink; P. M. Sberna; M. Rücker ; V. Garbin ; M. J. Serpe; H. Bazyar

APL Mater. 12, 091113 (2024)
https://doi.org/10.1063/5.0227483

AIP Publishing

APL Materials ARTICLE pubs.aip.org/aip/apm

Microgel-based etalon membranes: Characterization and properties

Cite as: APL Mater. 12, 091113 (2024); doi: 10.1063/5.0227483
Submitted: 9 July 2024 • Accepted: 26 August 2024 •
Published Online: 13 September 2024

View Online Export Citation CrossMark

G. Kontaxi,[1] G. Wensink,[2] P. M. Sberna,[3] M. Rücker,[2] V. Garbin,[1] M. J. Serpe,[4] and H. Bazyar[1,a)]

AFFILIATIONS

[1] Department of Chemical Engineering, Delft University of Technology, Delft, the Netherlands
[2] Department of Mechanical Engineering, Eindhoven University of Technology, Eindhoven, the Netherlands
[3] Department of Microelectronics, Delft University of Technology, Delft, the Netherlands
[4] Department of Chemistry, University of Alberta, Edmonton, Alberta T6G 2R3, Canada

[a)] **Author to whom correspondence should be addressed:** h.bazyar@tudelft.nl

ABSTRACT

We introduce Microgel-based Etalon Membranes (MEMs), based on the combination of stimuli-responsive microgels with an etalon, which is an optical device consisting of two reflecting plates and is used to filter specific wavelengths of light. The microgels are sandwiched between two reflective layers and, in response to a stimulus (e.g., temperature, pH, or biomarker concentration), swell or de-swell, thereby changing the distance between the two reflective layers and generating multiple peaks in the reflectance spectra. This property gives a MEM the unique capability of simultaneous separation and tunable responses to environmental changes and/or biomarker concentrations. We propose a design based on gold layers on a silicon nitride wafer membrane. Our comprehensive characterization, employing permeability experiments, *in situ* optical reflectance spectroscopy, in-liquid atomic force microscopy (AFM) analysis, and captive bubble contact angle measurements, elucidates the dynamic response of MEM to pH, temperature, and glucose stimuli and the corresponding effect of microgel swelling/de-swelling on the membrane properties, e.g., permeability. The AFM results confirm the dynamic changes of the microgel layer's thickness on the membrane surface in response to the stimuli. Although the microgel's swelling/de-swelling influences the effective pore radius, the decrease in the membrane's permeance is limited to less than 10%. In the swollen state of the microgels, the etalon membranes show a prominent hydrophilic behavior, while they become less hydrophilic in the microgels' de-swollen state. This work introduces MEM and provides novel insights into their behavior. The fundamental understanding that we reveal opens the way to applications ranging from point-of-care testing to continuous environmental monitoring.

I. INTRODUCTION

Functional systems capable of simultaneously separating and sensing a variety of analytes can be used in biomedical, pharmaceutical, and environmental monitoring. Integrating responsive microgels, which form optical sensors as microgel-based etalon structures, into inorganic membranes creates "smart" membranes that facilitate *in situ* separation and sensing. Fully understanding and characterizing these novel systems is crucial before their deployment in biomedical and environmental applications.

Membranes have attracted great scientific and industrial interest over the years as simple and energy-saving tools for separation and purification processes.[1] Nanofiltration (NF), ultrafiltration (UF), and microfiltration (MF) are prominent membrane-based separation processes for a variety of particle sizes. The pore diameter of the MF membranes is typically in the range of 0.1–6 μm, enabling the separation of proteins,[2] bacteria,[3] and blood cells[4] based on the principle of physical separation.[2,5] MF membranes have found applications in pharmaceuticals, wastewater treatment, as well as biotechnology.[2]

The challenge of optimizing the properties and performance of MF membranes, such as permeability, selectivity, and resistance to fouling, has led to various fabrication techniques and the use of both organic and non-organic materials.[6,7] Inorganic membranes fabricated with lithographic techniques have presented desirable properties, with silicon-oxide (SiO_2) and silicon-nitride (Si_3N_4)

being the main membrane materials.[2,8] SiO_2 and Si_3N_4 membranes have high temperature stability (>1000 °C), high resistance to acids, bases, and solvents, are recyclable, and can be sterilized. The given properties render them versatile materials for applications ranging from industrial processes and wastewater treatment to biomedical devices and environmental monitoring.[2,8,9] Si_3N_4 membranes have a higher Young's modulus (200 GPa[8]) compared to those of SiO_2 ones (70 GPa[10]), decreasing membrane deformation to achieve high strength and a flat surface. The Si_3N_4 membranes can thus operate at higher pressure ranges and fluxes, increasing their resistance to fouling.[4] Their chemical inertness, biocompatibility, and mechanical robustness render Si_3N_4 membranes an excellent candidate for filtration processes in wastewater treatment, gas separation, and biotechnological applications.[11–18]

Developing Si_3N_4 MF membranes via lithographic techniques can further enhance the properties and performance of MF membranes in micro-liquid handling and micro-analysis systems.[4] In this context, the modification of conventional membranes into "smart" membranes that respond to external stimuli will expand their use in a wider range of separation and sensing applications, such as controlled drug delivery, water treatment, bio-separation, and chemical sensors.[19,20] Smart membranes can be obtained using stimuli-responsive polymers by either embedding them in an existing membrane or directly fabricating a membrane from these polymers, where the membrane's properties (permeability or selectivity) can be dynamically controlled based on the surrounding conditions.[7,21–23]

Stimuli-responsive materials have raised significant attention due to their ability to undergo phase transition and exhibit mechanical response, making them valuable in various fields, e.g., drug delivery, self-healing coatings, and bio-separation.[24,25] Among these materials, stimuli-responsive microgels are aqueous, cross-linked, colloidal particles able to alter their solvation state in response to various stimuli.[26,27] One distinguishing feature of microgels is their capacity to swell or de-swell in response to a range of stimuli, such as changes in temperature, pH, light exposure, or ionic strength variations.[28] This responsiveness is typically reversible upon the removal of the stimulus.[29,30] The mechanical properties of microgel suspensions, as well as their sensitivity to specific stimuli, can be adjusted during their synthesis by modifying factors such as cross-linking density, polymer concentration, or the inclusion of co-monomers.[31] The direct control of these properties, combined with the biocompatibility of many microgels and their colloidal stability, makes them interesting candidates for potential applications in controlled drug delivery, tissue engineering, cell encapsulation, and as chemical and bio sensors.[26,31–33]

A variety of responsive microgels have been developed. Among them, aqueous thermo-responsive poly(N-isopropylacrylamide) (pNIPAm) microgels have been thoroughly investigated.[28] The temperature responsive pNIPAm-based microgels undergo a volume phase transition (VPT) when the temperature of the solvent reaches the lower critical solution temperature (LCST), at ~32 °C.[28,34] Below the LCST, the pNIPAm microgels are in the swollen state, where the hydrophilic segments of pNIPAm form hydrogen bonds with water molecules. Above the LCST, water is repelled from the crosslinked network, indicating weaker hydrogen bonds between the polymer and the water. The particles collapse, leading to the de-swollen state of the pNIPAm structure above the LCST.[28,32]

Microgels can be synthesized using various methods, such as free radical polymerization or precipitation polymerization.[30] The synthesis of pNIPAm microgels by precipitation polymerization provides colloidal particles with low polydispersity, controlled size (in the order of 50 nm to 1.5 μm in diameter in de-swollen and swollen states, respectively), and controlled functionalization.[35,36] During their synthesis, the addition of co-monomers, small molecules, or proteins into the microgels renders them multi-responsive, provoking alterations in their structure and function. Thermo-responsive pNIPAm-based microgels can be made pH-responsive by using acrylic acid (AAc) as a co-monomer.[37,38] At pH > pKa of AAc (≈4.25), the microgels are negatively charged and in their swollen state, while at pH < pKa the AAc groups are protonated and the microgels are in the de-swollen state, regaining full thermo-responsivity.[37,39] The attachment of molecules such as 3-aminophenylboronic acid (APBA) and N-[3-(dimethylamino)-propyl]methacrylamide (DMAPMA) to microgels' structure enables their responsivity to glucose and their application as drug-delivery systems, respectively.[29,35,37,40–42]

pNIPAM microgels offer the potential to fabricate color adjustable materials configuring an etalon structure. Etalon is an optical device comprising two flat mirrors separated by a dielectric layer, and it partially reflects/transmits specific wavelengths of light.[36,43,44] Monolithic thin-films of stimuli-responsive microgels (e.g., pNIPAm-co-AAc) enclosed between two gold-coated layers, supported on a glass substrate, form a microgel-based etalon structure that exhibits visible color and generates multiple peaks in the reflectance spectra.[36] Due to the size change of the microgels with temperature and pH, the color can be tuned due to the direct change of the mirror–mirror distance.[36,37] The position and the order of the peaks in the reflectance spectra depend on the distance between the two gold layers and the refractive index of the microgel,

$$\lambda = \frac{2nd\cos(\theta)}{m}, \tag{1}$$

where n is the refractive index of the dielectric layer, d is the mirror–mirror distance (nm), θ is the angle of incident light relative to the normal (°), and the integer m is the order of the reflected peak.[43] The change of the mirror–mirror distance, the refractive index of the dielectric layer, the angle of incident light, and/or the angle of observation correspond to a range of wavelengths. The shift in the position of the wavelength peak indicates the response of the microgels to the stimuli, denoting a change in the mirror–mirror distance influenced by their swelling/de-swelling.[41]

The integration of Si_3N_4 MF membranes with the stimuli-responsive microgels and etalon structures presents a holistic approach toward developing smart membranes with versatile applications in microfluidics. While individual components have been extensively studied, the integration of these elements into a unified smart membrane remains unexplored.

In this work, we introduce and evaluate the performance of Microgel-based Etalon Membranes (MEMs) based on using transparent gold coated Si_3N_4 membranes with etched pores in the range of 4 μm in diameter. pNIPAm-based microgels are spin coated on the gold layer, and a top gold layer is deposited upon the microgels, forming a microgel-based etalon membrane. AAc and APBA-functionalization of pNIPAm microgels render the etalons responsive to pH and glucose, respectively. Pure water permeability, *in situ* reflectance spectroscopy, contact angle (CA) measurements, and in-liquid atomic force microscopy (AFM) have been performed to fully characterize the MEM. During the permeability experiments, the pore radius of the etalon membranes is dynamically decreased with the microgel's response to the stimuli, which is optically detected, leading to a slight decrease in the membrane's permeance compared to that of the pristine membrane (2.4%–7.0% in the most de-swollen and swollen states of the microgel beads, respectively). A relation between the pore coverage by the microgel beads, the thickness of the monolithic microgel layer on the substrate, and the gap height of the microgel beads is established based on in-liquid AFM results. In-liquid AFM provides insight into the swelling and de-swelling dynamics of the microgel beads on the membrane surface. In all the studied cases, the linear pressure–flux relation and hydrophilic behavior (CA = 60.8°–91.2°) of the etalon membranes are maintained with less hydrophilicity in the de-swollen state of the microgel beads.

Responsiveness to multiple stimuli, dynamic tunability, real-time monitoring, and high sensitivity of the MEM lead to a unique functional membrane system with high accuracy and rapid diagnosis in a user-friendly platform. This work focuses on the detailed characterization and understanding of the fundamental properties of MEMs to enable their future use for rapid and on-site analysis of various biomarkers in biological samples, e.g., blood or urine, facilitating early disease detection and monitoring, rendering it a possible option in biomedical diagnostics and point-of-care testing. Their applications extend beyond the biomedical field, including environmental uses as well. Continuous monitoring of dissolved carbon dioxide (dCO_2) in seawater samples can be achieved by separating contaminants from seawater samples and providing real-time detection and concentration measurements of dCO_2, making MEM a valuable tool across multiple sectors where precise and efficient separation and detection are essential.

II. EXPERIMENTAL

A. Chemicals

Sodium hydroxide (NaOH) [reagent grade, ≥98%, pellets (anhydrous)], hydrochloric acid (HCl) (ACS reagent, 37%), sodium chloride (NaCl) (ACS reagent, ≥99.0%), α-D-glucose (ACS reagent), and APBA hydrochloride (98%) were obtained from Sigma-Aldrich, The Netherlands. Sodium bicarbonate ($NaHCO_3$) (ACS reagent, ≥99.7%) and sodium carbonate (Na_2CO_3) (ACS reagent, ≥99.5%) were also obtained from Sigma-Aldrich, The Netherlands. 1-Ethyl-3-(3-dimethylaminopropyl)carbodiimide hydrochloride (EDC), phosphate buffered saline (PBS (10X), pH 7.2), and BupH 2-(N-morpholino)ethanesulfonic acid (MES) buffered saline packets were obtained from Thermo Fisher Scientific Inc., The Netherlands, and were used as received or according to the package instructions. All deionized (DI) water had a resistivity of 18.2 MΩ cm and was obtained from a Milli-Q type 1 system from Merck KGaA, Germany.

B. Silicon nitride membrane fabrication

A microfabrication process is followed to fabricate Si_3N_4 MF membranes. Initially, a silicon nitride film (a thickness of 500 nm) is deposited on both sides of a n/phosphorous, double side polished, low resistivity (1–5 Ω cm), and ⟨100⟩ oriented silicon wafer of 525 ± 15 μm thickness by low-pressure chemical vapor deposition (LPCVD) (Tempress Systems Inc., S2T4, The Netherlands) at 860 °C with dichlorosilane (SiH_2Cl_2) and ammonia (NH_3). Then photoresist SPR3012 (a thickness of 2.1 μm) is spin coated on the silicon nitride wafer, and a soft bake at 95 °C for 90 s takes place. SUSS Micro-Tec MA/BA8 mask aligner and ultraviolet exposure are used to form membrane pores on the top surface of the wafer. Silicon window patterns are formed on the bottom surface through photoresist development. Dry etching of silicon nitride (500 nm deep) with hexafluoroethane (C_2F_6) gas is then performed for both pores and window patterns, followed by oxygen plasma exposure to remove the photoresist layer. Wet anisotropic potassium hydroxide (KOH) (33%) etching at 85 °C is performed to remove silicon in the window pattern on the bottom surface. Microfluidic membrane chips are obtained by dicing the silicon nitride wafer to square dimensions of 10×10 mm^2 with the porous membrane area (5×5 mm^2) in the center.

C. Microgel-based etalon membrane fabrication

The fabrication of the microgel-based etalon structure is similar to the previously published procedure.[37] Briefly, a layer of 10 nm Cr and 115 nm Au is evaporated on the membrane chips by physical vapor deposition (PVD) (CHA Industries, Inc., Solution PLC-S7). A 10 μl aliquot of pNIPAm-co-AAc microgels is spin coated at 3000 rpm for 30 s on the Au layer to create a homogeneous, monolithic film. The microgels are dried on the substrate for 2 h at 35 °C in the incubator and subsequently rinsed with deionized (DI) water to remove any excess microgels that is not directly bound to the Au layer. The samples are left in the incubator overnight at 30 °C, and a top layer of 2 nm Cr and 15 nm Au is evaporated on the microgel film to create the etalon structure.

Functionalization of the microgels with APBA is also performed on a set of MEMs, as described by Sorrell *et al.* to render them responsive to glucose.[40] The MEMs are placed in pH 4.7 MES buffered saline (Pierce, prepared based on the packet instructions), and 9 mg APBA is added to the buffer. The solution and sample are allowed to mix for 1 h on a magnetic stirrer at room temperature. 20 mg of EDC is further added to the buffered APBA solution and sample and stirred until EDC is fully dissolved. Subsequently, the solution and sample are left for 5 h in the refrigerator. An additional 4.5 mg of APBA is added per sample to the solution and mixed for 30 min on a magnetic stirrer. 20 mg of EDC are also added per sample and dissolved. The reaction takes place overnight at 4 °C. The samples are rinsed with deionized water and soaked in a 10 mM PBS buffer (with 150 mM ionic strength from NaCl) with a pH of 7.2 for 2 h to remove the unreacted reagents.

D. Permeability experiments

The permeability of both pristine and MEMs is studied using an experimental setup shown in Fig. 1. This setup consists of a pressure

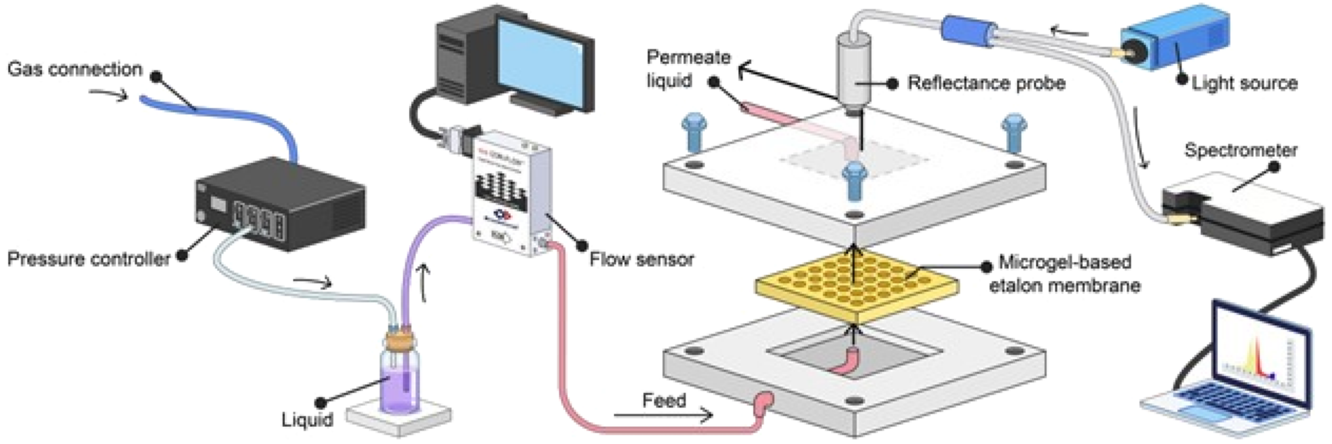

FIG. 1. Schematic representation of the experimental setup for membrane permeability and *in situ* reflectance spectroscopy measurements.

controller (Elveflow OB1 MK3+), a liquid flow meter (miniCORI-FLOW$^{\text{TM}}$ ML120V00), and a custom-built membrane module with a stainless-steel bottom plate and transparent PMMA top plate. In the bottom plate, a recess is designed with square dimensions of 10×10 mm^2 and a thickness of 500 μm for the precise fit of the membrane. The flow is driven from the bottom plate of the module perpendicularly to the membrane surface, indicating dead-end filtration operation. The experiments are conducted by stepwise pressure increase from 100 to 1200 mbar with steps of 100 mbar every 1 min and simultaneous measurement of the corresponding flow rate. The tested liquids are 1 mM DI water/NaCl of pH 6.5, 1 mM HCl/NaCl of pH 3.0, and 1 mM NaOH/NaCl of pH 11.0 for the pH- and T-stimuli responsive MEMs with1 mM ionic strength due to NaCl. The glucose responsive MEMs are tested with 5 mM $NaHCO_3$/Na_2CO_3 solution of pH 9.3[45] and 1 mM DI water/NaCl solution of pH 6.5 and glucose concentrations (C_g) of 50, 100, and 150 mg/dl. The tested liquids are at an ambient temperature of 22 °C, and for the experiments conducted at higher temperatures, the stainless-steel bottom plate is heated up to the desired temperature using a hot plate to maintain the steady temperature of the membrane. The permeability experiment at each temperature is performed three times for every membrane. The results demonstrate the average flux values every minute at each pressure with a standard deviation on the order of 10^{-1} L/m^{2}h.

E. *In situ* determination of etalon membrane response

Throughout the permeability experiments, *in situ* detection of the microgel response to the stimuli of interest is performed (Fig. 1, top). A UV/vis reflectance probe (Ocean Optics, SR2 UV-VIS, Florida) is placed on top of the PMMA top plate. Its distance from the module surface is adjusted for an optimal signal at 0.7 mm. The probe remains in the same position during each set of experiments to ensure that the spectra are recorded in the same manner. Once the liquid has permeated through the membrane, a spectrum is recorded by Ocean View 2.0 software with a wavelength range of 400–1000 nm. Reflectance spectra are recorded throughout the permeability experiments in total of three times for each liquid and temperature.

F. Captive bubble measurements

The hydrophilic/hydrophobic behavior of the etalon membranes is tested to further characterize the variations in membranes' wetting properties in the presence of stimuli. To resemble the conditions of the permeability experiments, contact angle measurements are performed while immersing etalon membranes in the test liquid. For this purpose, the captive bubble method is used to characterize the surface wetting properties of the MEM. The OCA25 contact angle machine (Dataphysics, Germany) is used for this measurement. A glass cell (Dataphysics, GC 50, Germany) is filled with the test solutions, and the etalon membrane is placed on a sample holder (Dataphysics, SHC 20, Germany), which is fitted into the GC 50 glass cell. An air bubble is injected beneath the etalon membrane, which is immersed in the liquid, using a bent stainless-steel needle (SNC 050/026) and the contact angle between the test liquid and the solid is measured using drop shape analysis. The obtained contact angle between the air bubble and the solid (θ_B) can be directly related to the water contact angle (θ_L) using the equation $\theta_L = 180° - \theta_B$.[46] The captive bubble contact angle measurements are conducted in liquids with different pH and glucose concentrations in a range of temperatures from 20 to 45 °C. The temperature of the test liquids is adjusted using a mercury thermometer with an accuracy of ±0.5 °C throughout the measurements. The sensitivity of the contact angle is 0.1°, and the experimental errors are less than 2.0°.

G. Scanning electron microscopy (SEM)

Microscopy images of the MEMs and the pristine membranes are taken with a JEOL 6010LA SEM. The cross section of a single pore is captured using focused ion beam (FIB) scanning electron microscopy (Thermo Scientific Helios 5 DualBeam).

TABLE I. Properties of ScanAsyst-fluid probe.

Property	Value
Nominal tip radius	20 nm
Cantilever length	70 μm
Cantilever width	10 μm
Spring constant	0.4 N/m

H. In-liquid atomic force microscopy (AFM)

To understand the effect of the microgel's response to stimuli on the microgel-based etalon membrane's permeance, in-liquid AFM is used (Bruker Nanowizard BioAFM equipped with a ScanAsyst-fluid probe). The properties of the probe are described in Table I. The thickness change of the monolithic microgel layer deposited on the membrane (t_E), the gap height change (h_G) between the two neighboring microgel beads, and the swelling/de-swelling dynamics of the microgels in response to different pH conditions are thoroughly investigated. The variations in the beads' stiffness in response to the stimuli are further obtained from Young's modulus (E) values when the etalon-membranes are immersed in liquids with different pH and glucose concentrations. A droplet of the solution is placed on the sample, after which the probe is brought into contact with the sample (Fig. 2). A 5 × 5 μm^2 area is scanned in Quantitative Imaging (QI)-mode imaging, and a 10 × 10 μm^2 area is scanned to obtain the swelling/de-swelling dynamic results. In this mode, force–distance curves are recorded in a 128 × 128 grid, and height profiles are extracted. Adaptive approach length is used, which determines the approach height based on the previously recorded curve. An initial approach length of 1 μm is used with a vertical tip velocity of 100 μm/s. The setpoint (maximum force on the surface) is 5 nN. Processing of the images is performed in the JPK data processing software (v8.0). A plane fit and line leveling are applied using a linear fitting procedure provided in the software with default settings. In each liquid, a different etalon membrane is used, and the measurements are performed three times under each condition.

III. RESULTS AND DISCUSSION

A. Microgel configuration in pore cavity

To depict the microgel deposition on the membrane surface, SEM is performed. The orientation of the membrane pores is demonstrated in Fig. 3(a). Membranes with 235 pores in hexagonal orientation and 4 μm diameter are tested. In Figs. 3(b) and 3(c), the monolithic layer of microgel beads around the pore is shown, and in a tilt position of the membrane, a "volcano" like structure is observed, creating the notion that microgels are deposited in the pore cavity. The cross-sectional SEM FIB images [Figs. 3(d) and 3(e)] confirm the notion, making it evident that the pore wall is also covered with the microgel beads. The effect of pore wall coverage by the beads on the membrane permeability is further studied (Sec. III D).

B. Analysis of microgel layer dynamics and mechanical properties via in-liquid AFM

To estimate the fraction of the beads covering the pore wall, the gap height between two neighboring beads and the thickness of the microgel layer in the presence of the stimuli are obtained using in-liquid AFM. To obtain the gap height between two beads of the microgel layer, a line segment crossing a bead with a relatively large spacing between neighboring beads was chosen, since the finite AFM tip size does not allow measurement of the gap between closely packed beads. The line crosses the apex of the bead to accurately measure its height. Figure 4 shows the gap height images obtained from QI-mode AFM experiments in 1 mM HCl/NaCl (pH 3.0), DI water/NaCl (pH 6.5), and NaOH/NaCl (pH 11.0) solutions. The beads immersed in NaOH solution have a larger apex height compared to that of the beads immersed in NaCl and HCl. The beads in all solutions have a similar base diameter, ranging from 725 to 790 nm depending on the swollen and de-swollen state of the beads as a response to pH (Fig. 4).

To calculate the thickness of the microgel layer in the presence of each stimulus, the surface was scratched, creating a gap between the monolithic layer of the microgel beads and the gold coated substrate. In Fig. 5, the thickness of the monolithic layer is presented for the three conditions (pH 3.0, 6.5, and 11.0) at 22 °C. The thickness

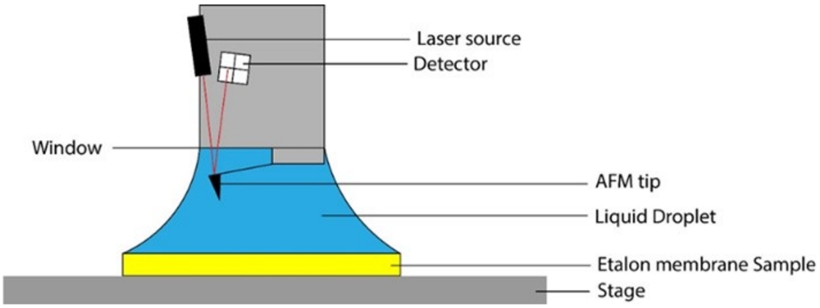

FIG. 2. Schematic concept of the in-liquid AFM measurements. A liquid droplet is placed on the sample and brought into contact with the AFM probe. A meniscus of liquid consequently forms between the sample and the AFM head. In this way, the sample and probe are continuously immersed during the measurement.

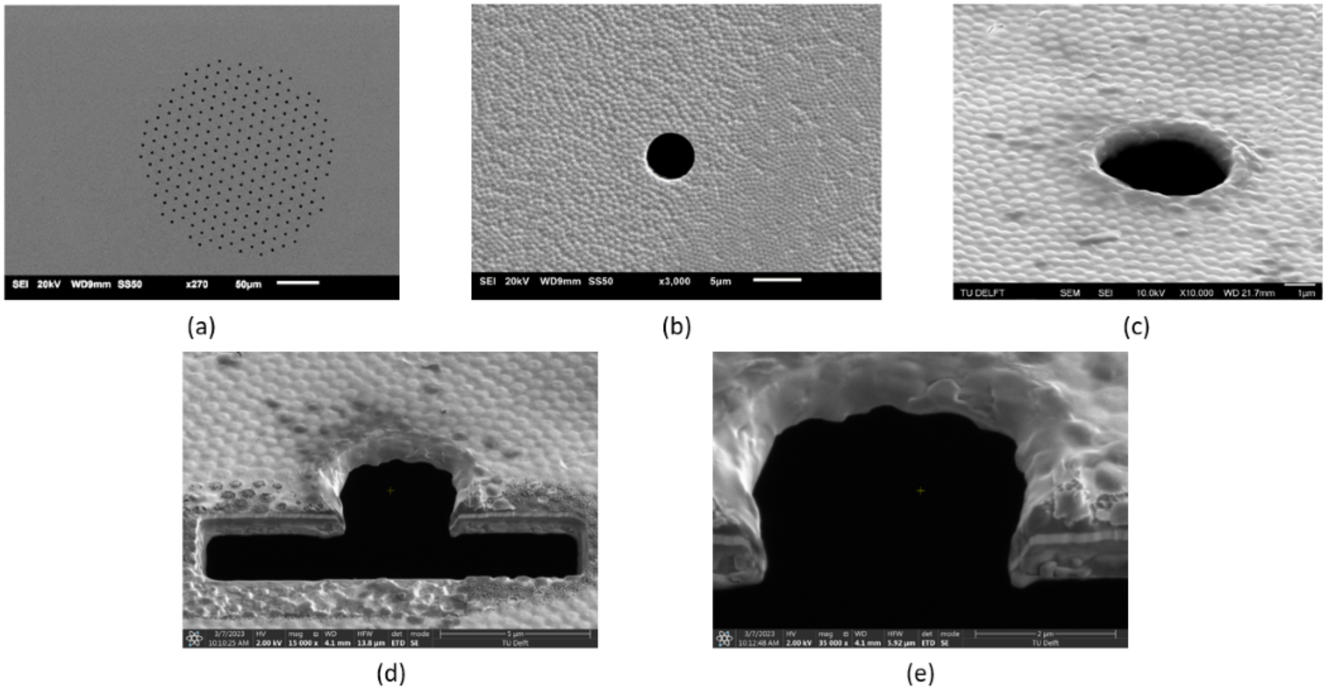

(a) (b) (c) (d) (e)

FIG. 3. SEM images of (a) the membrane area and (b) the monolithic microgel layer around the pore. SEM FIB images of (c) deposition of the microgel beads around the pore in a tilt position of the membrane, (d) and (e) cross section of the pore demonstrating the formation of a microgel layer on the pore wall.

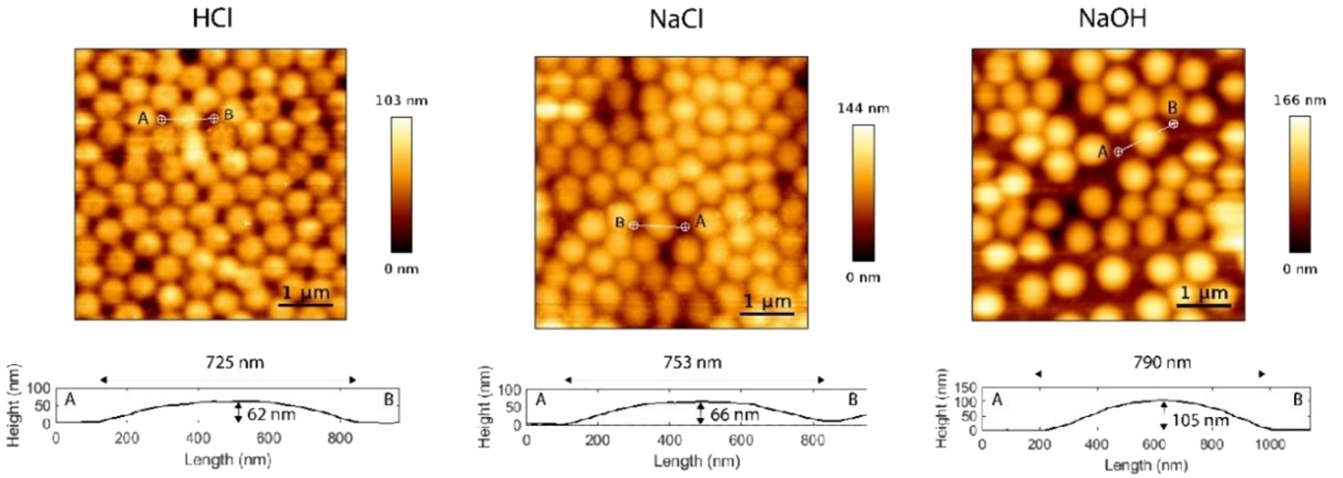

FIG. 4. Images of the microgel layer obtained from QI-mode when the MEMs are immersed in 1 mM HCl (pH 3.0), NaCl (pH 6.5), and NaOH (pH 11.0) solutions. A line segment from A to B is chosen in each image to extract the height profile of a single bead (gap height, h_G). These profiles are shown below the images, with point A on the left and point B on the right side of the graphs.

of three different locations under each condition is presented in the section titled "Effect of pH and temperature" of the supplementary material (Figs. S1–S3). In pH 3.0 (the most de-swollen state of the microgel beads), the monolithic layer of the beads shows a thickness of 387 nm. This thickness increases to 566 nm in the most swollen state at pH 11.0, which is almost equal to the thickness of the membrane (500 nm), doubling the thickness of the active membrane area.

The swelling/de-swelling dynamics of the microgels were tested by immersing the etalon membranes in solutions of pH 6.5 and 3.0, respectively. In Fig. 6, the thickness of the microgel layer is presented as a function of time. An increase of 20% in size is observed for the

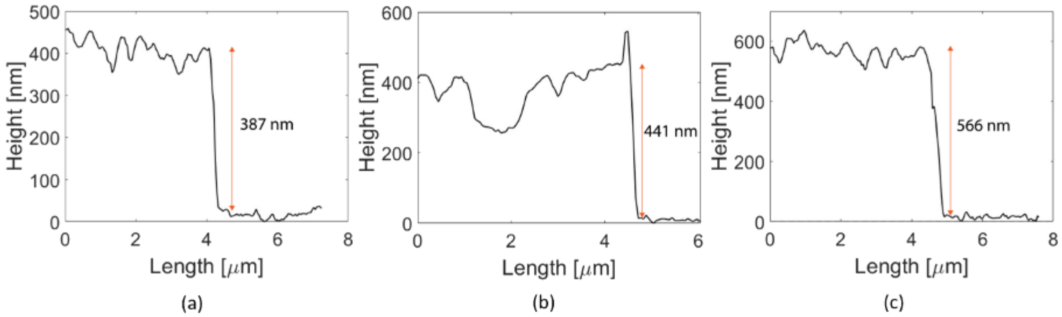

FIG. 5. Thickness of the microgel layer deposited on the membrane when immersed in 1 mM (a) HCl (pH 3.0), (b) NaCl (pH 6.5), and (c) NaOH (pH 11.0) solutions.

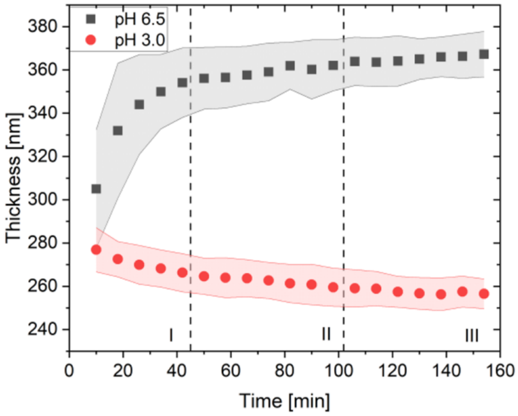

FIG. 6. Thickness of the microgel layer on the membrane's surface vs time when immersed in 1 mM HCl (pH 3.0) and NaCl (pH 6.5) solutions. Sections I, II, and III correspond to the dynamic response of the microgels to the stimuli. High rate observed in Sec. I, decrease in rate observed in Sec. II, and reaching a steady state in Sec. III.

TABLE II. Young's modulus values of the microgel beads immersed in liquids with different pH.

pH	Young's modulus (E) (MPa)
3.0	0.87 ± 0.76
6.5	0.45 ± 0.61
11.0	0.19 ± 0.32

microgels at pH 6.5 in a span of 2.5 h. The plot can be divided into three sections based on the response of the beads to the stimuli. An immediate response of the microgel beads to the stimuli is observed with a sharp initial swelling rate ($n = 1.45$) in the first 40 min (Sec. I), which gradually decreases between 40 and 106 min ($n = 0.13$, Sec. II) before reaching a steady state after 106 min ($n = 0.07$, Sec. III). In the de-swollen state (pH 3.0), the decrease in the microgel size reaches 7%, where again the decrease is more prominent during the first 40 min with a slope of $n = -0.32$ (Sec. I). A reduction in the de-swelling rate is observed in Sec. II ($n = -0.11$), and microgels' response comes to a steady state after 106 min ($n = -0.01$, Sec. III).

The Young's modulus of the microgel beads is further obtained via in-liquid AFM under different pH conditions to measure the stiffness of the microgels. As expected, the Young's modulus for the microgel beads in the de-swollen state at pH 3.0 is lower compared to that of the microgel beads in the swollen state when immersed in 1 mM DI water/NaCl (pH 6.5) and 1 mM NaOH/NaCl (pH 11.0) (Table II). This shows that the stiffness of the beads is affected by their response to the stimuli. In the de-swollen state, microgels undergo a volume phase transition accompanied by water expulsion, while in the swollen state, water is absorbed.[27] Hence, from the obtained Young's modulus values, it is noted that deformation of the beads as a response to pressure is highly likely to happen in the less stiff (swollen) state.

C. Effect of microgel beads on membrane pore size

Permeability experiments are conducted to characterize the performance of the MEM under different conditions. The maximum pressure that could be applied before the breaking point of the silicon nitride membrane is 1.2 bar. The effect of stimuli (pH and temperature) on the permeability performance of the MEM fabricated using pNIPAm-co-AAc microgels is tested and compared to that of the pristine membrane. The plot of permeating water flux as a function of the applied pressure is shown in Fig. 7. This plot is divided into two sections depending on the pressure range [Sec. I from 0.1 to 0.6 bar (low pressure) and Sec. II from 0.7 to 1.2 bar (high pressure)]. In Fig. 7(a) during the low-pressure range (Sec. I), the permeating flux through all etalon membranes aligns with that of the pristine membrane. This alignment indicates that the swelling/de-swelling behavior of the microgel beads causes negligible resistance to the flow through the pores in the low pressure range, even with pore wall coverage by the beads. As the pressure is increased (Sec. II), a deviation is observed between the permeating flux through the pristine and that through the etalon membranes. Section II in Fig. 7(a) is separately shown for pH and temperature in Figs. 7(b) and 7(c), respectively. Figure 7(b) shows the effect of the microgels' response to pH (3.0, 6.5, and 11.0 at 22 °C) on the permeating flux of the etalon membranes at high pressure, while Fig. 7(c) presents the effect of temperature (22, 40, 50, and 65 °C at pH 6.5). Particularly in Fig. 7(b), it is noticed that in the basic environment (swollen state), the impact of the pressure is more prominent. The

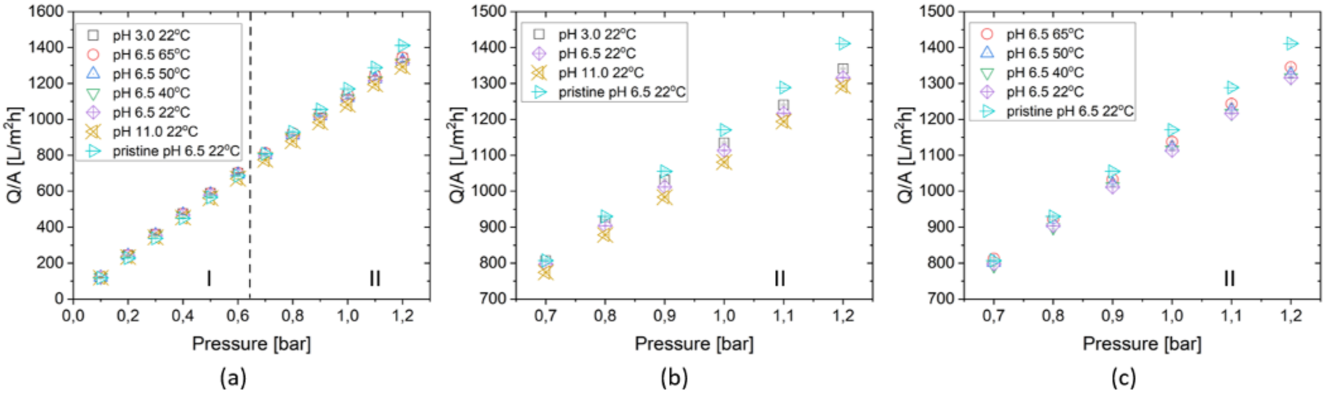

FIG. 7. (a) Comparison between the permeating water flux through the pristine membrane and that through the etalon membranes as a function of pressure at different pH and temperature ranges. Sections (I) and (II), respectively, correspond to low- and high-pressure regions. Effect of high pressure [Sec. (II) in plot (a)] on the permeating flux for the MEM under (b) different pH and (c) temperature conditions. Flux values for all the studied cases present a standard deviation of ±0.7 to ±8.2 L/m^{2}h.

TABLE III. Pore radius reduction, the thickness of the microgel layer covering the pore wall (δ), and percentage of the pore radius reduction (%Reduction) at P_{max} = 1.2 bar for three different pH conditions (3.0, 6.5, and 11.0) at 22 °C.

Condition	r_{et} (μm)	δ (μm)	%Reduction
pH 3.0	2.27	0.03	1.3
pH 6.5	2.26	0.04	1.8
pH 11.0	2.25	0.05	2.2

expansion of the beads due to water absorbance leads to a more elastic state of the microgels and coverage of a larger area in the pore cavity. From Young's modulus (Table II), it is shown that microgels in pH 11.0 (swollen state) are less stiff than in pH 3.0 (de-swollen state), explaining the increase in flux deviation of the etalon membranes from that of the pristine with an increase in pressure [Figs. 7(b) and 7(c)]. Thus, as the pressure increases, pore narrowing can be potentially expected, leading to a decrease in the flow rate compared to that of the pristine membrane. Similar behavior is observed in Fig. 7(c), where the impact of pressure on temperatures below LCST when the microgels are in the swollen (less stiff) state is obvious. Lower permeating flow rates through etalon membranes are observed at temperatures below LCST compared to temperatures above LCST (de-swollen and stiffer state of microgels). The greater deviation of the permeating flux of the etalon membranes in the swollen state from that of the pristine shows the variation of the microgel layer thickness covering the pore wall (δ) in response to the corresponding stimuli (Table III).

Thermo-responsive microgels with LCST behavior have presented pressure sensitivity in pressure ranges of 1–1000 bar.[47,48] The pressure sensitivity, of pNIPAm microgels emanates from temperature sensitivity leading to an increase in LCST with pressure and indicating the pressure dependence of VPT.[47] In this study, the experimental results show that the microgels response is affected by pressure at ranges from 0.7 to 1.2 bar, with the effect being more prominent in the swollen state of the microgels. In all the above cases, a linear relation between pressure and flux is obtained, showing that all the pores of the etalon membranes are open,[49,50] rendering them fully functional in both the swollen and de-swollen states of the microgels. The corresponding analysis of the logarithmic plot of flux as a function of pressure for the pristine and etalon membranes at different pH and temperatures is presented in the section titled "Effect of pH and temperature" of the supplementary material (Fig. S4).

The values of the permeating flux through MEM in the presence of various stimuli at high pressures [Figs. 7(b) and 7(c)] along with the pore wall coverage by the beads [Figs. 3(d) and 3(e)] lead to defining the "effective pore radius," which is dependent on the microgel response to the stimuli. The Hagen–Poiseuille law [Eq. (2)] is used to calculate the effective pore radius of the etalon membranes,[51]

$$Q = \frac{\pi r^4 \Delta P}{8\mu L}, \tag{2}$$

where μ (Pa s) is the dynamic viscosity, Q (m^3 s^{-1}) is the volumetric flow rate of the permeating fluid, and $\Delta P/L$ (Pa m^{-1}) is the pressure gradient across the membrane. Considering the equivalent pressure gradient for both pristine and etalon membranes, one can obtain Eq. (3) and calculate the effective pore radius at each pressure gradient. This radius is used to determine the difference with the pore radius of the pristine membrane (2.3 ± 0.05 μm), which is obtained from SEM images,

$$\frac{Q_p}{Q_{et}} = \frac{r_p^4}{r_{et}^4} \Rightarrow r_{et} = \sqrt[4]{\frac{r_p^4 Q_{et}}{Q_p}}, \tag{3}$$

where r_{et} and r_p (m) are the effective and initial pore radius, while Q_{et} and Q_p (m^3 s^{-1}) correspond to the liquid flow rate through the microgel-based etalon and pristine membranes, respectively.

The effect of the pressure on pore narrowing (reduction of pore radius) is presented in Table S1 (section titled "Effect of pH and temperature" of the supplementary material). With an increase in pressure, the pore radius of the MEM decreases under all the studied pH conditions. However, in the de-swollen state (pH 3.0), the

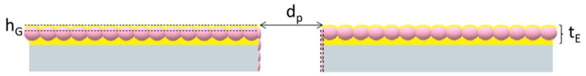

FIG. 8. Schematic representation of the beads deposition on the pore wall and the thickness relation (δ) with gap height (h_G) and thickness of the microgel layer on the substrate (t_E), where $\delta \approx \frac{1}{2}h_G \approx \frac{1}{10}t_E$ and d_p indicates the pore diameter.

narrowing of the pore is observed for pressures higher than 0.8 bar, reaching a decrease in pore radius of only 0.03 μm at maximum pressure (1.2 bar). This decrease is more pronounced when the microgels are in the swollen state (pH 6.5 and 11.0). The percentage of the pore radius reduction in the microgel-based etalon membrane compared to that of the pristine membrane at maximum pressure is shown in Table III. From SEM images, it is observed that a microgel layer is formed within the pore cavity. The thickness of the microgel layer covering the pore wall (δ) is calculated by subtracting the etalon pore radius [estimated by Eq. (3)] from that of pristine (2.3 ± 0.05 μm) at each pressure. The thickness of the microgel layer covering the pore wall (δ) at the maximum pressure under the studied pH conditions at 22 °C is presented in Table III. The thickness at pH 11.0 (most swollen state) is estimated to be 0.05 μm, leading to a maximum reduction of 2.2% in the pore radius.

Using the calculated thickness of the microgel layer within the pore at the maximum pressure (1.2 bar) (Table III), the measured gap height between two beads of the microgel layer (Fig. 4), and the thickness of the microgel layer on the surface (Fig. 5), the relation between these three parameters can be obtained (Fig. 8). The results show that the thickness of the microgel layer within the pore is almost half the gap height and one tenth of the overall thickness of the microgel layer on the surface. Figure 8 schematically shows how microgel beads cover the pore wall, indicating that microgels covering the pore wall do not provoke pore clogging even in the most swollen state of the beads. This further explains the slight decrease in the permeating flux through the MEM compared to that through the pristine membrane in the de-swollen state of the microgels and the greater deviation of flux values in the cases where the microgels are in the swollen state.

The results show that the MEMs exhibit tunable behavior, with microgels influencing pore radius and permeating flux under varying pH and temperature conditions. The swelling/de-swelling dynamics of microgel beads minimally affect flow in low pressures, while deviations in permeating flux emerge as pressure increases, especially in the swollen state. Despite deviations in permeability at higher pressures, the membranes consistently adhere to Darcy's prediction, affirming their functionality in both swollen and de-swollen states (section titled "Effect of pH and temperature" of the supplementary material). The thickness of the microgel layer within the pores leads to reductions in pore radius, particularly in the swollen state, emphasizing the combined effects of stimuli and pressure on the etalon membrane's characteristics.

D. Membrane permeance

The effective pore radius of the etalon membranes is used to study the permeability performance of the membranes. From Darcy's equation [Eq. (4)], the permeability of the membranes can be calculated by[52]

$$Q = \frac{\kappa A \Delta P}{\mu L} \Rightarrow \frac{Q}{A} = \frac{\kappa}{\mu L}\Delta P, \tag{4}$$

where Q/A ($m^3\ s^{-1}/m^2$) is the volumetric flux of the permeating fluid, κ (m^2) is the permeability, μ (Pa s) is the dynamic viscosity of the permeating fluid, and $\Delta P/L$ is the pressure gradient across the membrane thickness (Pa m^{-1}).

Due to the swelling/de-swelling behavior of the microgels as a response to stimuli, the thickness of the etalon membranes is dynamically changed. In some cases, etalon membranes showed a thickness two times larger than that of the pristine membrane [Figs. 5(b) and 5(c)]. Because the thickness and mechanical properties of the etalon membranes change with the stimuli (pH and temperature conditions), it is not possible to compare the permeability of the etalon and pristine membranes; rather, we compare the pressure-normalized flux or permeance [Eq. (5)]. Permeance, a membrane property, is commonly used in the case of composite membranes when the thickness is not known and/or varied,[53,54]

$$J = Pe \cdot \Delta P \Rightarrow Pe = \frac{J}{\Delta P}, \tag{5}$$

where J (L/m^2h) is the flux, ΔP (bar) is the pressure difference, and Pe (L/m^2hbar) is the pressure-normalized flux or permeance of the permeating liquid.

The pristine membrane presents the largest permeance value, obtained as a slope of the line from the flux vs pressure plot [Fig. 7(a)]. A reduction in permeance (compared to that of the pristine membrane) from 2.4% to 7.0% is noted for microgel-based etalon-membranes depending on the tested condition [different pH (3.0, 6.5, and 11.0)] at 22 °C and a variety of temperatures (40, 50, and 65 °C) in pH 6.5 (Table IV). At the most de-swollen state of the beads at pH 6.5 and 65 °C, a minimum decrease in permeance from that of the pristine is observed (2.4%), while at pH 3.0 and 22 °C, a 2.7% reduction is observed, showing a minimal decrease in the permeance in the de-swollen state of the microgels. At pH 11.0 and 22 °C, the beads are in the most swollen state, leading to an increase in the permeance reduction of 7.0%, indicating a more prominent effect on the membrane's performance. The temperature affects the etalon membranes' permeance (in pH 6.5) in a similar

TABLE IV. Permeance of the MEM under different conditions and percentage decrease in the MEM's permeance compared to that of the pristine membrane. The permeance is obtained as a slope of the line of flux vs pressure plot [Fig. 4(a)].

Condition	Permeance (L/m^2hbar)	%Reduction from pristine
pH 6.5 22 °C pristine	1173.3 ± 5	⋯
pH 11.0 22 °C	1093.7 ± 13.9	7.0%
pH 6.5 22 °C	1122.6 ± 18.6	4.4%
pH 6.5 40 °C	1124.9 ± 13.3	4.2%
pH 6.5 50 °C	1130.4 ± 18.4	3.7%
pH 3.0 22 °C	1141.7 ± 16.1	2.7%
pH 6.5 65 °C	1145.9 ± 17.4	2.4%

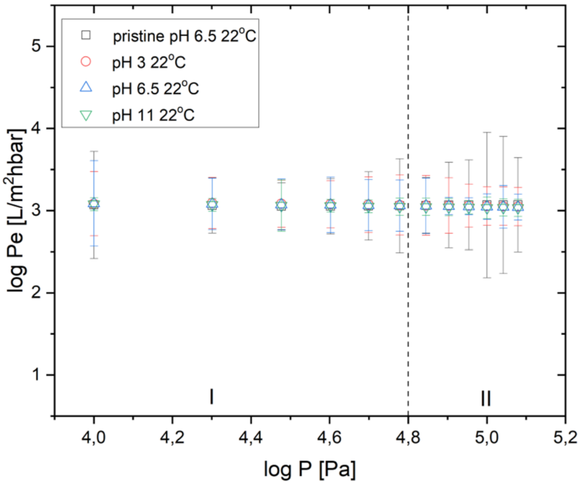

FIG. 9. Logarithmic plot of permeance as a function of pressure for the pristine and etalon membranes under different pH conditions. The S.D. of the obtained values of permeance is in a range of ±0.08 to ±0.9 [L/m^{2}hbar].

TABLE V. Contact angle (CA) of MEM based on captive bubble measurements for different pH and temperature values.

Temperature (°C)	CA(°) pH 3.0	CA(°) pH 6.5	CA(°) pH 11.0
20	83.1 ± 0.3	68.4 ± 0.7	60.8 ± 0.4
25	83.5 ± 1.1	78.8 ± 0.5	63.9 ± 0.2
30	84.1 ± 0.1	80.6 ± 0.4	64.4 ± 0.2
35	86.6 ± 0.3	81.8 ± 0.7	65.4 ± 0.1
40	87.2 ± 0.2	82.9 ± 0.5	67.4 ± 0.2
45	91.2 ± 0.1	84.7 ± 0.6	69.1 ± 0.6

manner. At 22 °C (swollen state of the microgel beads), the permeance difference from that of the pristine reaches 4.4%, while at 50 °C the beads are in a de-swollen state, leading to 3.7% of permeance reduction.

The response of the microgel beads to the stimuli (swelling/de-swelling) does not provoke deviation of the etalon membranes' permeance from Darcy's law (see Fig. S4 and section titled "Effect of pH and temperature" of the supplementary material). The response of the microgels to pH [Fig. S4(A)] and temperature [Fig. S4(B)] does not affect the linear relation of flux with pressure as it is predicted from Darcy's equation. The logarithm of the pristine and etalon membranes' permeance under three different pH conditions as a function of pressure is shown in Fig. 9. The results show constant values of permeance in low pressures (Sec. I from 0.1–0.6 bar) for both pristine and etalon membranes, indicating that there is no resistance in the liquid flow for all the studied conditions. In high pressures (Sec. II from 0.7–1.2 bar), a slight decrease in the permeance values is obtained for the etalon membranes compared to the pristine ones, showing that the presence of microgels within the pore wall constitutes a barrier to the liquid flow without significantly affecting the membrane's performance.

E. Wetting properties

The changes in the surface wetting properties (hydrophilic/hydrophobic behavior) of the etalon membranes under different conditions (pH 3.0, 6.5, and 11.0 at various temperatures) are studied using captive bubble measurements (Table V). The results show that under all the pH conditions, the contact angle increases with an increase in temperature, demonstrating a less hydrophilic behavior of the etalon membrane. This behavior is observed at temperatures above the LCST compared to temperatures below the LCST. This corresponds to the de-swelling behavior of the beads in temperatures above the LCST, where the hydrophobic isopropyl domains of pNIPAm are in contact with water and polymer segments.[55,56] In particular, in pH 3.0, where the microgels are in the most de-swollen state at 45 °C, the contact angle reaches around 91° [Fig. 11(a)]. In the most swollen state of the beads [pH 11.0 and 20 °C (below the LCST)], the beads show a hydrophilic behavior, leading to a contact angle of around 60° [Fig. 11(b)]. Noteworthy, since the pNIPAm microgels are hydrophilic in nature, the beads and the membranes show hydrophilic behavior in general, even in the de-swollen state.[55]

F. *In situ* optical sensing of microgel response to stimuli

During the permeability experiments, *in situ* reflectance spectroscopy is performed to study the microgel's response to the stimuli (swelling/de-swelling). The swelling/de-swelling behavior of the microgels to pH and temperature changes result in an increase/decrease in the distance between the two gold layers, leading to a peak shift in the wavelength, which was successfully detected by reflectance spectroscopy (see Fig. S5 and the section titled "Effect of pH and temperature" of the supplementary material). The maximum wavelength peak and peak shift for different pH and temperatures at 0.9 bar are presented in Fig. 11. At pH 3.0 (<pKa of AAc), the microgel beads are in the de-swollen state, leading to a peak shift from 635 nm (in pH 6.5) to 588 nm (blue shift). In the basic environment of pH 11.0, a red shift is observed (the peak shift increases to 649 nm from the peak in pH 6.5), indicating the swelling of the microgels [Fig. 10(a)]. A blue shift of the microgels is also observed with an increase in the temperature from 22 °C (635 nm) to 65 °C (606 nm) at pH 6.5 [Fig. 10(b)]. The results indicate that our MEM can respond to the desired stimuli during water permeability experiments.

G. Effect of glucose

Permeability and reflectance spectroscopy experiments were also performed with MEM responsive to glucose. Glucose buffer solutions were prepared with pH 9.3 (5 mM $NaHCO_3/Na_2CO_3$) and pH 6.5 (1 mM DI water/NaCl) with glucose concentrations (C_g) of 50, 100, and 150 mg/dl. All the experiments were performed at 22 and 37 °C. The ultimate scope was to study the performance of the MEM in pH 6.5 and 37 °C to resemble the conditions inside a human body. The results are shown in the section titled "Effect of glucose" of the supplementary material.

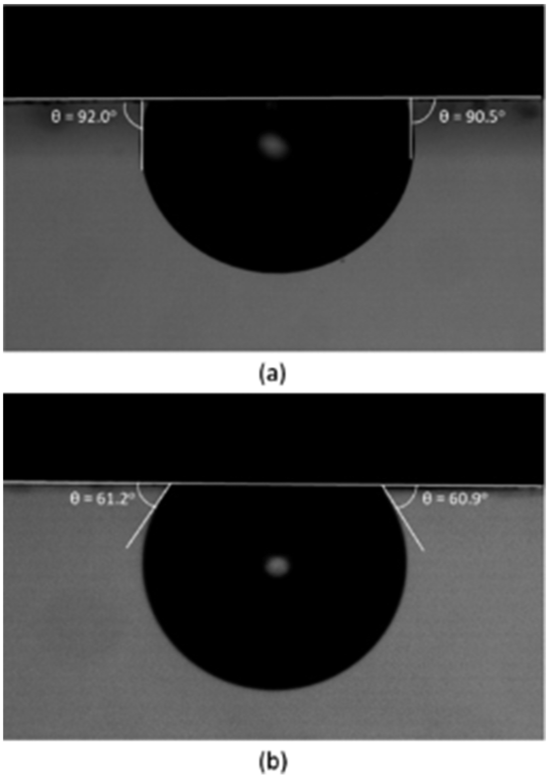

FIG. 10. Contact angle measured by the captive bubble method for microgel-based etalon membrane immersed in (a) 0.01M HCl solution at 45 °C (pH 3.0), where microgels are in the most de-swollen state; and (b) 0.01M NaOH solution at 20 °C (pH 11.0), with microgels being in the most swollen state. (The obtained contact angle between the air bubble and the solid (θ_B) is related to the water contact angle (θ_L) with the equation $\theta_L = 180° - \theta_B$).

In permeability studies, a linear relation between permeated flux through the membrane and pressure is observed (Figs. S6A and S9A). Deviation of the flux values from those of the pristine membranes was observed at high pressures (0.6–1.2 bar) [Figs. S6(B), S6(C), S9(B), and S9(C)], similar to the performance of the pH- and temperature-responsive etalon membranes. The permeance of the etalon membranes was affected by the response of the beads to the glucose concentration. In the most swollen state of the beads (150 mg/dl glucose concentration at pH 9.3 and 22 °C), the maximum permeance decrease of 12.5% was observed compared to that of the pristine (Table S2). The decrease in the etalon membranes' permeance from that of the pristine at pH 6.5 and 37 °C, for the three tested glucose concentrations, was within a range of 5.2%–7.7% (Table S3). This further shows that the binding of glucose to the boronic acid groups of the APBA is favored in a basic environment, where boron is in its negatively charged state due to the hydroxylation of the boron atoms.[57,58] The binding of glucose to boronic acid groups increases the Coulombic repulsion inside the microgel, leading to the swollen state of the microgels. However, at high temperatures, the hydrophobicity of the functionalized polymer prevails over the elevated Coulombic repulsion inside the microgel, resulting in a rise in the Volume Phase Transition Temperature (VPTT) compared to that of pNIPAm (32 °C).[40,57] At pH 9.3 and 37 °C, there is a decrease in etalon membranes' permeance compared to that of the pristine from 6.1% to 10.7%, with an increase in glucose concentration (Table S2) indicating that the swelling behavior of the beads is more prominent even though the temperature is higher than the LCST.

The hydrophilic/hydrophobic behavior of the glucose-responsive etalon membranes is also studied by captive bubble measurements for different glucose concentrations in pH 9.3 and 6.5 at 22 and 37 °C. By increasing glucose concentration, the microgels swell further, leading to a reduced CA. This indicates a more hydrophilic behavior of the membranes, with a minimum

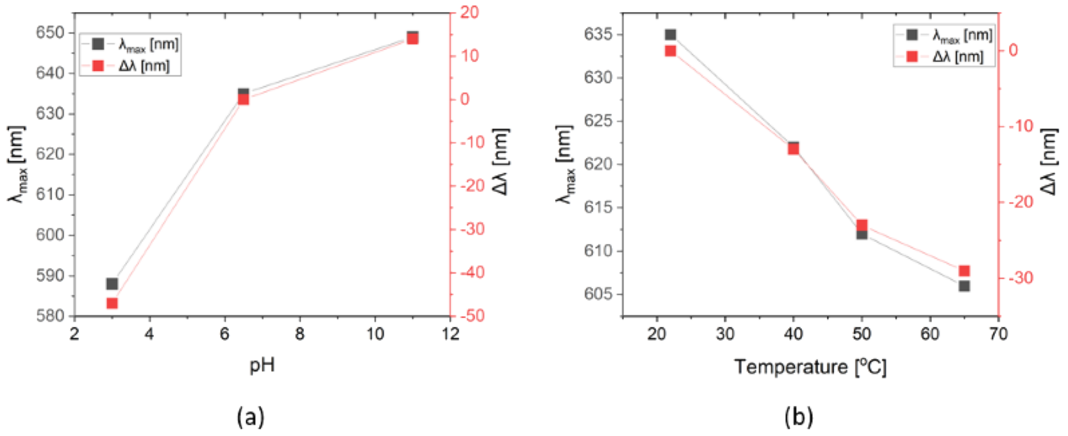

FIG. 11. Maximum wavelength peak and peak shift obtained from *in situ* reflectance spectra of the pNIPAm-co-AAc MEM during permeability experiments (P = 0.9 bar) in different (a) pH values (T = 22 °C) and (b) temperature values at pH 6.5. The negative values of $\Delta\lambda$ in the plots demonstrate the blue shift due to the de-swelling of the microgels from pH 6.5 to pH 3.0 (a) and with an increase in temperature (b), with $\Delta\lambda = \lambda_{testcondition} - \lambda_{\text{pH 6.5, 22°C}}$.

value of around 36° for C_g = 150 mg/dl at 20 °C and pH 9.3 (most swollen state) (Table S4). The effect of temperature is also noticeable, leading to an increase in CA values with a maximum of around 69° for C_g = 50 mg/dl at 45 °C and pH 6.5 (least swollen) (Table S5). The APBA functionalized etalon membranes for all the tested glucose concentrations at pH 9.3 have lower CA values, indicating that the swollen response of the beads when bound to glucose in a basic solution is more prominent than solely the response of the beads to a basic buffer. However, the hydrophilicity of the APBA functionalized beads decreases at pH 6.5 and in temperatures above the LCST, leading to similar CA values with the non-APBA-functionalized microgels at pH 11.0.

The *in situ* reflectance spectroscopy was performed during the permeability experiments [Figs. S8(A), S8(B), S11(A), and S11(B)]. A red shift was observed in the reflectance spectra at all the studied glucose concentrations and conditions, indicating the swelling behavior of the microgel beads. At a pressure of 0.9 bar, the larger peak shift (60 nm) was observed for C_g = 150 mg/dl at pH 9.3 and 22 °C ($\lambda_{\max}$ = 695 nm compared to $\lambda_{\max}$ = 635 nm for C_g = 0 mg/dl at pH 9.3 and 22 °C) [Fig. 12(a)]. In Fig. 12(b), at pH 6.5 and 37 °C, a smaller peak shift (21 nm) was observed for C_g = 150 mg/dl with $\lambda_{\max}$ = 630 nm. This indicates that the swelling response of the APBA functionalized microgels is more pronounced in the basic buffer, while the increase in temperature above the LCST acts like a counter force to the swelling response of the beads. The calibration curve for glucose concentration up to 300 mg/dl in solutions of pH 9.3 and 6.5 at 22 °C (Fig. S12) shows that the response of the APBA functionalized microgels is more sensitive at pH higher than the pKa of boronic acid moieties (pKa = 8.2) on the APBA.[40]

The performance of APBA-functionalized MEM could render them a potential candidate for *in situ* separation-sensing microfluidic devices to detect glucose levels in the blood. The increase in hydrophilicity of the membrane's surface as well as the red shift observed by reflectance spectroscopy with the increase in the glucose concentration in the buffers demonstrates the sensing capabilities of the device. The response of the microgels to the glucose concentration leads to only a slight decrease in the permeance of the etalon membranes compared to the pristine ones, supporting the feasibility of separation of red blood cells from plasma for future applications to on-site analysis and monitoring of glucose level in the blood.

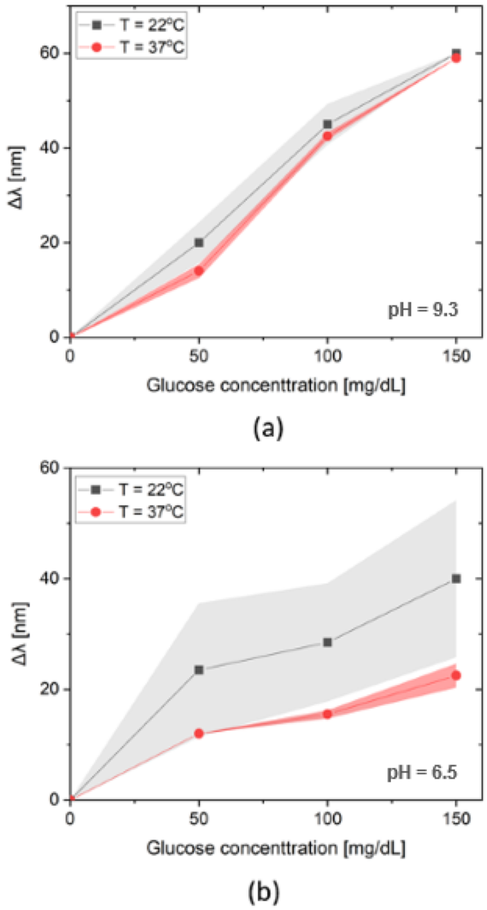

FIG. 12. Wavelength peak shift vs glucose concentration during permeability experiments (P = 0.9 bar) at 22 and 37 °C for (a) pH 9.3 and (b) pH 6.5, including shaded error bars.

IV. CONCLUSION

This work addresses the challenges of combining membranes and responsive elements into a multifunctional system capable of both permeating liquid and sensing. Our study centered on the comprehensive characterization of MEMs, providing insights into their physical and functional properties. The permeability experiments, supported by *in situ* reflectance spectroscopy and captive bubble contact angle measurements, provided a detailed understanding of the membranes' behavior under different pH, temperatures, and glucose concentrations. We observed a linear relation between permeating water flux and pressure, affirming the open functionality of the etalon membranes' pores. The effective pore radius was shown to be influenced by the microgels' response to stimuli, resulting in pore narrowing with increased pressure. The thickness of the microgel layer within the pore was found to impact the etalon membrane's permeance, with a decrease of 2.4%–7.0% compared to that of the pristine membrane, revealing its significance in governing the overall performance. A decrease in the hydrophilicity was observed in the de-swollen state of the microgels. In-depth AFM analysis revealed that the gap height between microgel beads and the thickness of the monolithic layer depends on their response to the stimuli, while dynamic changes in microgel size were observed over time. The swelling/de-swelling response led to a peak shift in the wavelength, detected by reflectance spectroscopy. These results show the stability and functionality of the MEM under various stimuli.

Our work establishes a relationship between the structural aspects of the microgel layer and the functional performance of the membrane, paving the way toward smart membranes with potential applications in separation-sensing microfluidic technologies. These fundamental understandings demonstrate that MEMs represent a significant advancement, leaving space for follow up studies with real blood samples and their response to target metabolites such as glucose and lactate. This study not only contributes valuable insights into the stimuli-responsive behavior of MEM but also underscores their promising prospects in responsive membrane technologies, contributing to the advancement of diagnostic and analytical tools.

SUPPLEMENTARY MATERIAL

The supplementary material provides results regarding the effect of pH and temperature on the relation of flux with pressure, the effect of the pressure on pore narrowing, and the reflectance spectra during permeability experiments. The in depth characterization of the glucose responsive MEMs is also presented, including results of permeability, reflectance spectroscopy, and contact angle measurements.

ACKNOWLEDGMENTS

We thank Nicholas Balasuriya from the University of Alberta, Canada, for preparing the microgel suspensions. We thank Daniel Tam's group and Bob Mulder from Delft University of Technology, the Netherlands, for providing the design of the membrane chips. We thank Burak Eral's group from Delft University of Technology, the Netherlands, for providing the equipment for the contact angle measurements. We also thank the Peyman Taheri's group for providing the equipment for FIB-SEM and Mohammad Soleimani for his help.

AUTHOR DECLARATIONS

Conflict of Interest

The authors have no conflicts to disclose.

Author Contributions

G. Kontaxi: Data curation (lead); Formal analysis (lead); Investigation (lead); Methodology (lead); Writing – original draft (lead). **G. Wensink**: Investigation (supporting). **P. M. Sberna**: Methodology (supporting). **M. Rücker**: Supervision (supporting). **V. Garbin**: Writing – review & editing (supporting). **M. J. Serpe**: Conceptualization (supporting); Supervision (supporting); Writing – review & editing (supporting). **H. Bazyar**: Conceptualization (lead); Supervision (lead); Writing – review & editing (lead).

DATA AVAILABILITY

The data that support the findings of this study are openly available in the 4TU repository.

REFERENCES

[1] Z.-G. Wang, L.-S. Wan, and Z.-K. Xu, "Surface engineerings of polyacrylonitrile-based asymmetric membranes towards biomedical applications: An overview," J. Membr. Sci. **304**, 8–23 (2007).

[2] S. F. Anis, R. Hashaikeh, and N. Hilal, "Microfiltration membrane processes: A review of research trends over the past decade," J. Water Process Eng. **32**, 100941 (2019).

[3] A. T. Nguyen, R. Van Doorn, J. Baggerman, J. M. J. Paulusse, M. M. Klerks, H. Zuilhof, and C. J. M. Van Rijn, "Flow-through microbial capture by antibody-coated microsieves," Adv. Mater. Interfaces **2**, 1400292 (2015).

[4] S. Kuiper, C. Van Rijn, W. Nijdam, and M. Elwenspoek, "Development and applications of very high flux microfiltration membranes," J. Membr. Sci. **150**, 1–8 (1998).

[5] A. F. Ismail and P. S. Goh, "Microfiltration membrane," in *Encyclopedia of Polymeric Nanomaterials*, edited by S. Kobayashi and K. Müllen (Springer Berlin Heidelberg, Berlin, Heidelberg, 2015), pp. 1250–1255.

[6] W. Eykamp,"Chapter 1 microfiltration and ultrafiltration," in *Membrane Science and Technology* (Elsevier, 1995), Vol. 2, pp. 1–43.

[7] M. Barth, M. Wiese, W. Ogieglo, D. Go, A. J. Kuehne, and M. Wessling, "Monolayer microgel composite membranes with tunable permeability," J. Membr. Sci. **555**, 473–482 (2018).

[8] M. Ghaderi and R. F. Wolffenbuttel, "Design and fabrication of ultrathin silicon-nitride membranes for use in UV-visible airgap-based MEMS optical filters," J. Phys.: Conf. Ser. **757**, 012032 (2016).

[9] *Inorganic Membranes: Synthesis, Characterization and Applications*, 1st ed., *Membrane Science and Technology Series Vol. 13*, edited by E. M. Society, R. Mallada, and M. Menéndez (Elsevier, Amsterdam; Boston, MA, 2008).

[10] J. Thurn and R. F. Cook, "Stress hysteresis during thermal cycling of plasma-enhanced chemical vapor deposited silicon oxide films," J. Appl. Phys. **91**, 1988–1992 (2002).

[11] C. van Rijn, W. Nijdam, and M. Elwenspoek, "High flow rate microsieve for bio medical applications," J. Dyn. Syst., Meas., Control **57-2**, 995–1000 (1995).

[12] Y. Quan, Z. Zhu, D. Tang, S. Zhu, C. Wang, K. Chen, and Z. Ni, "An ultra-thin silicon nitride membrane for label-free CTCs isolation from whole blood with low WBC residue," Sep. Purif. Technol. **296**, 121349 (2022).

[13] F. L. Riley, "Silicon nitride and related materials," J. Am. Ceram. Soc. **83**, 245–265 (2004).

[14] E. Wright, J. J. Miller, M. Csordas, A. R. Gosselin, J. A. Carter, J. L. McGrath, D. R. Latulippe, and J. A. Roussie, "Development of isoporous microslit silicon nitride membranes for sterile filtration applications," Biotechnol. Bioeng. **117**, 879–885 (2020).

[15] J. P. S. DesOrmeaux, J. D. Winans, S. E. Wayson, T. R. Gaborski, T. S. Khire, C. C. Striemer, and J. L. McGrath, "Nanoporous silicon nitride membranes fabricated from porous nanocrystalline silicon templates," Nanoscale **6**, 10798–10805 (2014).

[16] J.-W. Zhang, H. Fang, J.-W. Wang, L.-Y. Hao, X. Xu, and C.-S. Chen, "Preparation and characterization of silicon nitride hollow fiber membranes for seawater desalination," J. Membr. Sci. **450**, 197–206 (2014).

[17] H. Abadikhah, C.-N. Zou, Y.-Z. Hao, J.-W. Wang, L. Lin, S. A. Khan, X. Xu, C.-S. Chen, and S. Agathopoulos, "Application of asymmetric Si_3N_4 hollow fiber membrane for cross-flow microfiltration of oily waste water," J. Eur. Ceram. Soc. **38**, 4384–4394 (2018).

[18] H. D. Tong, H. V. Jansen, V. J. Gadgil, C. G. Bostan, E. Berenschot, C. J. M. Van Rijn, and M. Elwenspoek, "Silicon nitride nanosieve membrane," Nano Lett. **4**, 283–287 (2004).

[19] L.-B. Zou, J.-Y. Gong, X.-J. Ju, Z. Liu, W. Wang, R. Xie, and L.-Y. Chu, "Smart membranes for biomedical applications," Chin. J. Chem. Eng. **49**, 34–45 (2022).

[20] Y. Pan, Y. Liu, S. Yang, C. Zhang, and Z. Ullah, "Recent research progress on the stimuli-responsive smart membrane: A review," Nanotechnol. Rev. **12**, 20220538 (2023).

[21] M. Dirksen, P. Fandrich, L. Goett-Zink, J. Cremer, D. Anselmetti, and T. Hellweg, "Thermoresponsive microgel-based free-standing membranes: Influence of different microgel cross-linkers on membrane function," Langmuir **38**, 638–651 (2022).

[22] D. Wandera, S. R. Wickramasinghe, and S. M. Husson, "Stimuli-responsive membranes," J. Membr. Sci. **357**, 6–35 (2010).

[23] L. Chu, Y. Li, J. Zhu, and W. Chen, "Negatively thermoresponsive membranes with functional gates driven by zipper-type hydrogen-bonding interactions," Angew. Chem., Int. Ed. **44**, 2124–2127 (2005).

[24] M. A. C. Stuart, W. T. S. Huck, J. Genzer, M. Müller, C. Ober, M. Stamm, G. B. Sukhorukov, I. Szleifer, V. V. Tsukruk, M. Urban, F. A. Winnik, S. Zauscher, I. Luzinov, and S. Minko, "Emerging applications of stimuli-responsive polymer materials," Nat. Mater. **9**, 101–113 (2010).

[25] C. L. Bayer and N. A. Peppas, "Advances in recognitive, conductive and responsive delivery systems," J. Controlled Release **132**, 216–221 (2008).

[26] G. Agrawal and R. Agrawal, "Stimuli-responsive microgels and microgel-based systems: Advances in the exploitation of microgel colloidal properties and their interfacial activity," Polymers **10**, 418 (2018).

[27] X. Li, Y. Gao, and M. Serpe, "Stimuli-responsive assemblies for sensing applications," Gels **2**, 8 (2016).

[28] S. Wellert, M. Richter, T. Hellweg, R. von Klitzing, and Y. Hertle, "Responsive microgels at surfaces and interfaces," Z. Phys. Chem. **229**, 1225–1250 (2015).

[29] Y. Gao, X. Li, and M. J. Serpe, "Stimuli-responsive microgel-based etalons for optical sensing," RSC Adv. **5**, 44074–44087 (2015).

[30] R. Pelton, "Temperature-sensitive aqueous microgels," Adv. Colloid Interface Sci. **85**, 1–33 (2000).

[31] H. M. Wyss, J. Mattsson, T. Franke, A. Fernandez-Nieves, and D. A. Weitz, "Mechanics of single microgel particles," in *Microgel Suspensions*, 1st ed., edited by A. Fernandez-Nieves, H. M. Wyss, J. Mattsson, and D. A. Weitz (Wiley, 2011), pp. 311–325.

[32] S. J. Lue, B.-W. Chen, C.-M. Shih, F.-Y. Chou, J.-Y. Lai, and W.-Y. Chiu, "Micron- and nano-sized poly(N-isopropylacrylamide-co-acrylic acid) latex syntheses and their applications for controlled drug release," J. Nanosci. Nanotechnol. **13**, 5305–5315 (2013).

[33] L. P. Guerzoni, J. C. Rose, D. B. Gehlen, A. Jans, T. Haraszti, M. Wessling, A. J. Kuehne, and L. De Laporte, "Cell encapsulation in soft, anisometric poly(ethylene) glycol microgels using a novel radical-free microfluidic system," Small **15**, 1900692 (2019).

[34] L. D. Taylor and L. D. Cerankowski, "Preparation of films exhibiting a balanced temperature dependence to permeation by aqueous solutions—A study of lower consolute behavior," J. Polym. Sci., Polym. Chem. Ed. **13**, 2551–2570 (1975).

[35] C. D. Sorrell and M. J. Serpe, "Reflection order selectivity of color-tunable poly(N-isopropylacrylamide) microgel based etalons," Adv. Mater. **23**, 4088–4092 (2011).

[36] C. D. Sorrell, M. C. D. Carter, and M. J. Serpe, "A "paint-on" protocol for the facile assembly of uniform microgel coatings for color tunable etalon fabrication," ACS Appl. Mater. Interfaces **3**, 1140–1147 (2011).

[37] C. D. Sorrell, M. C. D. Carter, and M. J. Serpe, "Color tunable poly (N-Isopropylacrylamide)-co-Acrylic acid microgel-Au hybrid assemblies," Adv. Funct. Mater. **21**, 425–433 (2011).

[38] K. Kratz, T. Hellweg, and W. Eimer, "Influence of charge density on the swelling of colloidal poly(N-isopropylacrylamide-co-acrylic acid) microgels," Colloids Surf., A **170**, 137–149 (2000).

[39] J. Zhang, L.-Y. Chu, Y.-K. Li, and Y. M. Lee, "Dual thermo- and pH-sensitive poly(N-isopropylacrylamide-co-acrylic acid) hydrogels with rapid response behaviors," Polymer **48**, 1718–1728 (2007).

[40] C. D. Sorrell and M. J. Serpe, "Glucose sensitive poly (N-isopropylacrylamide) microgel based etalons," Anal. Bioanal. Chem. **402**, 2385–2393 (2012).

[41] Q. M. Zhang, W. Xu, and M. J. Serpe, "Optical devices constructed from multiresponsive microgels," Angew. Chem., Int. Ed. **53**, 4827–4831 (2014).

[42] Y. Gao, A. Ahiabu, and M. J. Serpe, "Controlled drug release from the aggregation–disaggregation behavior of pH-responsive microgels," ACS Appl. Mater. Interfaces **6**, 13749–13756 (2014).

[43] G. Brooker, *Modern Classical Optics*, *Oxford Master Series in Physics No. 8* (Oxford University Press, Oxford; New York, 2003), oCLC: ocm52829216.

[44] M. Deetlefs, K. R. Seddon, and M. Shara, "Neoteric optical media for refractive index determination of gems and minerals," New J. Chem. **30**, 317 (2006).

[45] G. E. Delory and E. J. King, "A sodium carbonate-bicarbonate buffer for alkaline phosphatases," Biochem. J. **39**, 245 (1945).

[46] A. V. Prydatko, L. A. Belyaeva, L. Jiang, L. M. C. Lima, and G. F. Schneider, "Contact angle measurement of free-standing square-millimeter single-layer graphene," Nat. Commun. **9**, 4185 (2018).

[47] X. Zhong, Y.-X. Wang, and S.-C. Wang, "Pressure dependence of the volume phase-transition of temperature-sensitive gels," Chem. Eng. Sci. **51**, 3235–3239 (1996).

[48] E. Kato, T. Kitada, and C. Nakamoto, "Anomalous compressibility of N-isopropylacrylamide gels near the volume phase transition temperature," Macromolecules **26**, 1758–1760 (1993).

[49] M. Mietton-Peuchot, "Use of gas-liquid porometry measurements for selection of microfiltration membranes," J. Membr. Sci. **133**, 73–82 (1997).

[50] H. Bazyar, S. Javadpour, and R. G. H. Lammertink, "On the gating mechanism of slippery liquid infused porous membranes," Adv. Mater. Interfaces **3**, 1600025 (2016).

[51] G. Hagen, "Ueber die Bewegung des Wassers in engen cylindrischen Röhren," Ann. Phys. **122**, 423–442 (1839).

[52] H. Darcy, *Les fontaines publiques de la vile de Dijon* (V. Dalmont, Paris, 1856).

[53] R. W. Baker, *Membrane Technology and Applications*, 1st ed. (Wiley, 2012).

[54] J. D. Seader, E. J. Henley, and D. K. Roper, *Separation Process Principles with Applications Using Process Simulators*, 3rd ed. (Wiley, Somerset, 2011), oCLC: 1020029390.

[55] R. Pelton, "Poly(N-isopropylacrylamide) (PNIPAM) is never hydrophobic," J. Colloid Interface Sci. **348**, 673–674 (2010).

[56] B. Jean, L.-T. Lee, and B. Cabane, "Interactions of sodium dodecyl sulfate with acrylamide-*N*-isopropylacrylamide) statistical copolymer," Colloid Polym. Sci. **278**, 764–770 (2000).

[57] T. Hoare and R. Pelton, "Engineering glucose swelling responses in poly (*N*-isopropylacrylamide)-based microgels," Macromolecules **40**, 670–678 (2007).

[58] G. Springsteen and B. Wang, "A detailed examination of boronic acid–diol complexation," Tetrahedron **58**, 5291–5300 (2002).